Internal Tides Energy Transfers and Interactions with the Mesoscale Circulation in Two Contrasted Areas of the North Atlantic

Adrien Bella, Noé Lahaye, Gilles Tissot

Internal tides energy transfers and interactions with the mesoscale circulation in two contrasted areas of the North Atlantic.

Adrien Bella, Noé Lahaye, Gilles Tissot

INRIA Rennes Bretagne Atlantique, IRMAR – UMR CNRS 6625, av. General Leclerc, 35042 Rennes, France

December 21, 2023

Abstract

The energy budget of the internal tide and its life cycle is investigated with a high resolution numerical simulation and a vertical normal mode decomposition. Two areas of interest are considered: the Azores Islands over the mid Atlantic ridge and the Gulf Stream offshore the North of the US East coast shelf break. Low mode (1 and 2) internal tides are found to propagate from 100 km (mode 2) to 1000 km (mode 1) away from their generation sites. Waves loose a significant portion of their energy as they propagate through the Gulf Stream, in contrast to the Azores domain. In the Gulf Stream domain, the mesoscale circulation is responsible for energy transfers from low to high modes internal tides, while the topographic scattering is dominant in the Azores area. This transfer of energy toward high modes favours energy dissipation. The mesoscale is significant in the energy budget of modes higher than mode 1 for both domains, and for all baroclinic modes in the Gulf Stream area. The internal tide is found to extract or loss energy toward the mesoscale circulation, but this accounts for less than 14%, of the energy scattered from low internal tide modes to higher ones once summed over all contributions of the modal energy budget.

Keywords— Internal tide, mesoscale flow, energy budget, vertical modal decomposition, high resolution numerical simulation.

1 Introduction

Internal tides are a category of oceanic internal inertia-gravity waves that are generated when the astronomical tide interacts with topographic features such as shelf breaks, ridges or seamounts. They are encountered in many areas in the ocean [Zaron et al., 2022, Zhao et al., 2016, among others] and are of crucial importance for the mixing of deep water and the closure of the Meridional Overturning circulation [Munk and Wunsch, 1998]. The role of mesoscale currents for the energy pathway starting from the barotropic tide input and leading to this mixing is not yet fully understood. As a different thread of motivation, internal tides exhibit the same spatial scale as (sub-)mesoscale features, which renders challenging the estimation of the geostrophic velocities and the disentanglement of the two type of motions from satellite altimetry ([Ponte and Klein, 2015]). This problem is exacerbated by the ability of the new SWOT mission to obtain a resolution of 20 km to 30 km, compared to the approximately 100 km of current altimeter products (Ballarotta et al. [2019]). It is therefore needed to better understand the dynamics of the internal tide if we hope to disentangle them from the geostrophic field via data assimilation for instance.

Since a decade or so [*e.g.* Arbic et al., 2010], global and regional realistic simulations have reached a sufficient resolution to be able to represent both internal tides and mesoscale features, opening the way to studying their interactions. Most studies focusing on these interactions use the vertical modal decomposition framework [Gill, 1982], which allows to get a clear separation of the barotropic and

baroclinic tides as well as alleviating the computational cost associated with processing 3D simulation outputs.

The importance of the mesoscale circulation and buoyancy field have been shown by [Kelly and Lermusiaux, 2016] in a realistic configuration over the Gulf Stream area for the energy budget of the first baroclinic mode (denoted mode 1). They quantified the energy transfers between the mode 1 and the mesoscale circulation as well as its relative importance compared to topographic effects, showing that the mesoscale explains first order interactions pattern visible on the mode 1 energy flux divergence. Similarly, [Pan et al., 2021] have analysed the energy budget of the mode 1 in a realistic setup including the mesoscale circulation and heterogeneous buoyancy field in the Gulf Stream area and the Mallau Island, leading to the same conclusion concerning the importance of mesoscale - internal tides interactions. Both studies have also considered realistic simulations with baroclinic currents, and have used a modal decomposition approach to define their energy budget. The deviation of internal tide energy flux have been analysed by [Duda et al., 2018], indicating a refracting behaviour of a Gulf Stream like current on beams of internal tides energy fluxes. [Dunphy and Lamb, 2014] have shown in an idealised setup that the interactions of the first baroclinic internal tide mode with the barotropic eddy and the first baroclinic eddy mode lead to a modification of the energy flux propagation and a scattering of energy toward higher modes, respectively.

In the present paper, our focus will be on the energy budget yielded by a modal analysis and we will in particular extend the work of other studies to the 10 first baroclinic modes, as well as studying the couplings between modes.

The contribution of the mesoscale flow and buoyancy field will be taken into account and the relative importance of the coupling between modes as well as their spatial pattern will be quantified in an area where topographic feature are prominent, and another area with a strong mesoscale circulation.

The document is organised as follows: section 2 will explain the theoretical framework with the modal decomposition and the governing dynamical equations. Section 3 will detail the dataset used and computational techniques. Section 4 will present results. Section 5 closes this article with a conclusion.

2 Governing equations and energy budget

To investigate the modal internal tide energy budget, we rely on linearized equations of motions projected on vertical normal modes. The derivation follows previous studies (*e.g.* Kelly and Lermusiaux [2016]) and is only briefly depicted here. It starts from the hydrostatic primitive equations under the Boussinesq approximation with a free surface [*e.g.* Vallis, 2017]:

$$\partial_t \boldsymbol{u}_h + \boldsymbol{u}\cdot\boldsymbol{\nabla}\boldsymbol{u}_h + f\vec{e_z}\wedge\boldsymbol{u}_h = -\boldsymbol{\nabla}_h p - \boldsymbol{\nabla}\Pi_{\text{tide}}, \tag{1a}$$

$$\partial_z p - b = 0, \tag{1b}$$

$$\partial_t b + \boldsymbol{u}\cdot\boldsymbol{\nabla} b = 0, \tag{1c}$$

$$\boldsymbol{\nabla}\cdot\boldsymbol{u} = 0, \tag{1d}$$

where $\boldsymbol{u}$ is the velocity, b the buoyancy, p the reduced pressure (divided by ρ_0, the reference density), and the index h denotes horizontal component of a 3D vector. Other variable names follow standard notations. Here, the forcing and dissipation terms have been omitted on purpose, except for the tidal potential term Π_{tide}.

Next, the flow is decomposed into low-frequency mesoscale flow and a high-frequency component that includes the internal tide: *i.e.*, for the velocity, we split $\boldsymbol{u} = \boldsymbol{U} + \tilde{\boldsymbol{u}}$. We will further decompose the slow variables of the buoyancy into a long-time mean and a slow variable part: $B = \bar{B} + B'$ ($\bar{\cdot}$ denotes long time average), and introduce the Brunt-Väisälä frequency: $N^2 = \partial_z B$ and $\bar{N}^2 = \partial_z \bar{B}$. Subtracting the low frequency equations (1) to the initial system and further assuming that nonlinearities amongst the high-frequency flow are negligible, one obtains the following linear system of equations:

$$\partial_t \tilde{\boldsymbol{u}} + \boldsymbol{U}\cdot\boldsymbol{\nabla}\tilde{\boldsymbol{u}} + \tilde{\boldsymbol{u}}\cdot\boldsymbol{\nabla}\boldsymbol{U} + f\vec{e_z}\wedge\tilde{\boldsymbol{u}} = -\boldsymbol{\nabla}\tilde{p} - \boldsymbol{\nabla}\Pi_{\text{tide}}, \tag{2a}$$

$$\partial_z \tilde{p} - \tilde{b} = 0, \tag{2b}$$

$$\partial_t \tilde{b} + \boldsymbol{U}\cdot\boldsymbol{\nabla}\tilde{b} + \tilde{\boldsymbol{u}}_h\cdot\boldsymbol{\nabla}_h(\bar{B} + B') + \tilde{w}(\bar{N}^2 + N'^2) = 0, \tag{2c}$$

$$\boldsymbol{\nabla}\cdot\tilde{\boldsymbol{u}} = 0. \tag{2d}$$

Note that, since the above system of equations is linear in the high-frequency variables, and assuming that most of the mesoscale variability is of timescale longer or equal to the cutoff period used in the internal tides complex demodulation (3 days), band-pass filtering of these equations leaves the system

unchanged. Hence, in our study, we will focus on the semi diurnal (including M2 and S2 frequencies) internal tide with a period centred on 12.2 h, relying on the above set of equations where the high-frequency variables describe this frequency band. These equations are completed by the usual linearized boundary conditions at the mean surface $\overline{\eta}$ and the bottom at $z = -H$:

$$\tilde{p}(\overline{\eta}) = g\tilde{\eta}, \tag{3}$$

$$\tilde{w}(\overline{\eta}) = \partial_t(\tilde{\eta}) + \boldsymbol{U}_h(\overline{\eta}) \cdot \boldsymbol{\nabla}_h(\tilde{\eta}), \tag{4}$$

$$\tilde{w} = -\tilde{\boldsymbol{u}}_h(-H) \cdot \boldsymbol{\nabla} H. \tag{5}$$

We thus have the internal tide part of the primitives equations that are now ready to be projected on a set of verticals modes. The latter are given locally by the standard Sturm-Liouville problem for internal waves in a rotating stratified ocean [*e.g.* Gill, 1982, Vallis, 2017], assuming a flat ocean, a horizontally-homogeneous stratification profile and no background flow:

$$\left(\frac{\Phi_n^{'}}{\bar{N}^2}\right)^{'} + \frac{\Phi_n}{c_n^2} = 0, \quad \text{with} \quad \Phi_n^{'} = 0 \text{ at } z = -H, \quad \text{and} \quad g\Phi_n^{'} + \bar{N}^2\Phi_n = 0 \text{ at } z = \overline{\eta}, \tag{6}$$

where prime denotes vertical derivative. The obtained set of vertical modes Φ_n is complemented by another set of vertical functions which obey:

$$\varphi_n^{'} = \Phi_n, \ \Phi_n{}^{'} = -\frac{\bar{N}^2}{c_n^2}\varphi_n, \tag{7}$$

and these modes follow the orthogonality conditions:

$$\int_{-H}^{\overline{\eta}} \Phi_m\Phi_n \, \mathrm{d}z = \int_{-H}^{\overline{\eta}} \frac{\bar{N}^2}{c_n^2}\varphi_m\varphi_n \, \mathrm{d}z + \frac{g}{c_n^2}, \varphi_m(\overline{\eta})\varphi_n(\overline{\eta}) = H\delta_{mn}. \tag{8}$$

Physical fields can then be expanded over these bases through:

$$[\boldsymbol{u}_h, p] = \sum_n [\boldsymbol{u}_n, p_n]\Phi_n, \tag{9}$$

$$[w, b] = \sum_n [w_n, \bar{N}^2 b_n]\varphi_n, \tag{10}$$

and the modal projection coefficient are obtained as follows:

$$[\boldsymbol{u}_n, p_n] = \langle [\boldsymbol{u}_h, p], \Phi_n \rangle \, , \tag{11}$$

$$w_n = \frac{1}{c_n^2}\left(\langle \varphi_n, w\bar{N}^2 \rangle + \frac{g}{H} w(\overline{\eta})\varphi_n(\overline{\eta})\right), \tag{12}$$

$$b_n = \frac{1}{c_n^2}\left(\langle \varphi_n, b \rangle + \frac{g}{H}\frac{b(\overline{\eta})}{\bar{N}^2(\overline{\eta})}\varphi_n(\overline{\eta})\right), \tag{13}$$

with the inner product defined as such: $\langle f, g \rangle = \frac{1}{H}\int_{-H}^{\overline{\eta}} f(z)g(z) \, \mathrm{d}z$. Note that the two bases have a parametric dependency on the horizontal coordinates because of the varying topography $H(x, y)$ and stratification profile $\bar{N}^2(z; x, y)$. In this paper, we are going to consider the modes 0 to 10, with the mode 0 being the barotropic tide, and all others being the baroclinic internal tide.

The dynamical equations are then obtained by projecting the tidal momentum equations and continuity on a mode Φ_m, and buoyancy equations on the mode φ_m, using the relation exposed above plus integration by part and Leibniz formula, and substituting the buoyancy modal amplitude by the pressure anomaly (after projection of the hydrostatic balance on φ_m) [Kelly and Lermusiaux, 2016, Kelly, 2016, Pan et al., 2021]. Omitting the $\tilde{\cdot}$ notation from now on, one obtains – after a tedious but

straightforward derivation:

$$\partial_t \boldsymbol{u}_m + \boldsymbol{\nabla}_h p_m + f\vec{e_z} \wedge \boldsymbol{u}_m = -\sum_n U_{mn} \cdot \boldsymbol{\nabla} \boldsymbol{u}_n - \sum_n \boldsymbol{u}_n U^{\Phi}_{mn} - \sum_n \boldsymbol{u}_n \cdot U^{\boldsymbol{\nabla}}_{mn} - \sum_n w_n U^z_{mn} - \sum_n p_n T_{mn} - \frac{1}{H} \boldsymbol{\nabla} \Pi_{\text{tide}}(\varphi_m(\overline{\eta}) - \varphi_m(-H)), \tag{14a}$$

$$\partial_t p_m - c_m^2 w_m = -\frac{g}{H} \varphi_m(\overline{\eta}) \boldsymbol{U}_h(\overline{\eta}) \cdot \boldsymbol{\nabla} \eta - \sum_n U^p_{mn} \cdot \boldsymbol{\nabla} p_n - \sum_n p_n \left\langle \varphi_m, \boldsymbol{U}_h \cdot \boldsymbol{\nabla} \left(\frac{\bar{N}^2}{c_n^2} \varphi_n \right) \right\rangle + \sum_n \boldsymbol{u}_n \cdot (B_{mn} - \bar{B}_{mn}) + \sum_n w_n \left\langle \varphi_m, \varphi_n N^2 \right\rangle, \tag{14b}$$

$$\boldsymbol{\nabla}_h \cdot (H \boldsymbol{u}_m) + H w_m = H \sum_n \boldsymbol{u}_n T_{mn}, \tag{14c}$$

with:

$$T_{mn} = \langle \Phi_m, \boldsymbol{\nabla}_h \Phi_n \rangle, \qquad U_{mn} = \langle \Phi_m, \boldsymbol{U}_h \Phi_n \rangle, \qquad U^{\Phi}_{mn} = \langle \Phi_m, \boldsymbol{U}_h \cdot \boldsymbol{\nabla}_h \Phi_n \rangle,$$
$$U^{\boldsymbol{\nabla}}_{mn} = \langle \Phi_m, \Phi_n \boldsymbol{\nabla} \boldsymbol{U}_h \rangle, \qquad U^z_{mn} = \langle \Phi_m, \varphi_n \partial_z \boldsymbol{U}_h \rangle, \qquad U^p_{mn} = \left\langle \varphi_m, \boldsymbol{U_{tot}} \frac{\bar{N}^2}{c_n^2} \varphi_n \right\rangle,$$
$$B_{mn} = \langle \varphi_m, \Phi_n \boldsymbol{\nabla} B \rangle, \qquad \bar{B}_{mn} = \left\langle \varphi_m, \Phi_n \boldsymbol{\nabla}_h \bar{B} \right\rangle.$$

We then take the scalar product of the projected momentum equation (14a) with $\boldsymbol{u}_n$ and multiply the pressure equation (14b) with p_m, substitute w_n using the continuity equation (14c) to obtain the energy budget of the internal tide mode m in presence of a slowly varying mesoscale circulation and buoyancy field:

$$\overbrace{\frac{\partial}{\partial t}\left(\frac{\boldsymbol{u}_m^2}{2} + \frac{p_m^2}{2c_m^2}\right)}^{\text{temporal variation of energy}} + \overbrace{\frac{1}{H}\boldsymbol{\nabla}_h \cdot (H \boldsymbol{u}_m p_m)}^{\text{divergence of energy flux}} =$$
$$-\sum_n \Big[\overbrace{\boldsymbol{u}_m \cdot (U_{mn} \cdot \boldsymbol{\nabla} \boldsymbol{u}_n) - \boldsymbol{u}_m \cdot \boldsymbol{u}_n U^{\Phi}_{mn} + \frac{p_m}{c_m^2} U^p_{mn} \cdot \boldsymbol{\nabla} p_n}^{\text{advection by the background flow}} - \overbrace{\boldsymbol{u}_n \cdot U^{\boldsymbol{\nabla}}_{mn} \cdot \boldsymbol{u}_m + \boldsymbol{u}_m \cdot U^z_{mn} w_n}^{\text{Background flow shear}}$$
$$+ \overbrace{\frac{p_m}{H c_m^2} \boldsymbol{u}_n \cdot (\bar{B}_{mn} + B_{mn})}^{\text{horizontal gradient of background buoyancy}} + \overbrace{\frac{p_m}{c_m^2} w_n \left\langle \varphi_m, N^2 \varphi_n \right\rangle}^{\text{slowly variable stratification}} + \overbrace{p_m \boldsymbol{u}_n \cdot T_{nm} - p_n \boldsymbol{u}_m \cdot T_{mn}}^{\text{Topography and mean stratification: } C_{mn}} \Big] + R_m \tag{15}$$

with

$$R_m = \overbrace{-\frac{p_m}{H c_m^2} g \varphi_m(\overline{\eta}) \boldsymbol{U_h}(\overline{\eta}) \cdot \boldsymbol{\nabla} \tilde{\eta}}^{\text{advection of ssh by the background flow}} - \sum_n \overbrace{\frac{p_m}{c_m^2} \sum_n p_n \left\langle \varphi_m, \boldsymbol{U}_h \cdot \boldsymbol{\nabla}_h \left(\frac{\bar{N}^2}{c_n^2} \varphi_n \right) \right\rangle}^{\text{advection of mean stratification by the background flow}}$$
$$- \overbrace{\boldsymbol{u}_m \cdot \boldsymbol{\nabla} \Pi_{tide}(\varphi_m(\overline{\eta}) - \varphi_m(-H))}^{\text{Tidal potential work}}. \tag{16}$$

By anticipation of the results in figure 3 in section 4.2, the term R_m gathers all contributions that are not of primary importance (and will not be discussed in this paper).

This equation describes the different energy exchanges (coupling) between modes as well as energy sources and sinks. Most coupling terms can be represented with coupling matrices –noted K_{mn} here – that will be shown below in section 4.2 (Figure 2). Generally, this coupling matrix contains an anti-symmetric part, describing net exchanges of energy between modes, and a symmetric part, with the diagonal included, that describes gain/loss of energy for the internal tide.

The first three terms in the right-hand side (RHS) arise from the presence of a mesoscale flow, while the next two ones include contributions from associated buoyancy perturbations as well as seasonal variations. The term labelled as slowly variable stratification, arises during the derivation of the CSW buoyancy equation 14 because of our choice to construct the modal bases by using a stationary profile of stratification in the problem 6. In case of a definition of the vertical modal bases with the instantaneous stratification profile, this term would vanish. Indeed, for a linear propagation of an internal wave without

topography, mesoscale and dissipation, the vertical modes diagonalise the operator, thus decouples the components from each other. By time-averaging the stratification profile, the associated vertical mode basis becomes inadequate to perform this decoupling. The slowly variable stratification term then arises, taking into account in the energy equation coupling between modes associated with this linear propagation. This term can be interpreted as energy exchanges between modes during a linear propagation of an internal wave without topography, mesoscale and dissipation. Since vertical modes are eigenfunctions of this associated idealised operator, we associate the variable stratification term to the inadequacy of the basis to represent internal wave dynamics (through the time-averaged stratification profile). We do not expect, however, that using a basis defined with a slowly time-varying stratification would change significantly the magnitude of the dominant interaction terms discussed in this paper (see e.g. section 4.2), and in particular the mesoscale and topographic contributions.

Finally, $C_{mn} = -C_{nm}$ is the topographic scattering, which includes the generation of baroclinic tide from the barotropic tide (C_{m0}). Note that this term has no symmetric part – it can only redistribute energy amongst the vertical modes.

Once averaged in time over a sufficiently long period (typically, one month), the time-variation of the energy vanishes and the above modal energy equation reduces to the following, simplified form:

$$\boldsymbol{\nabla}_h \mathbf{F}_m = -\sum_n K_{mn} + R_m, \tag{17}$$

where $\mathbf{F}_m$ denotes the modal energy flux, K_{mn} gathers the energy transfers, sources and sinks that are not negligible and R_m gathers all the neglected terms. These include a contribution from the free surface and the tidal potential, which would both vanish under a rigid-lid assumption for the baroclinic modes – in agreement with the fact that we find they have negligible magnitude in our diagnostics (cf. Sect. 4). The remaining term in R_m involves horizontal variations of the modes and associated background stratification, which is small since a year average is used.

3 Data and method

3.1 eNATL60 simulation

The high-resolution realistic simulation of the North Atlantic Ocean eNATL60 [Brodeau et al., 2020] is used to diagnose the energy budget of the internal tide following eq. (15). It uses the Nucleus for European Modelling of the Ocean (NEMO) model, which solves the primitive equations under the Boussinesq and hydrostatic approximations with an Arakawa C grid and z-coordinate with partial step [Madec and the NEMO team, 2008]. The eNATL60 run includes astronomical tidal forcing with the M2, S2, N2, O1 and K1 frequencies. In addition, surface forcing from the 3-hourly ERA-interim (ECMWF) reanalysis is used, which enables the simulation to develop a realistic mesoscale field. The horizontal resolution of the simulation is $1/60^\circ$ (about 1.5 km in the mid latitudes) and features 300 vertical levels with a thickness starting from less than 1 m at the top of the ocean to 100 m at the bottom. We processed the hourly outputs of the horizontal velocity $\boldsymbol{u}$, sea level, temperature and salinity fields (from which we computed the pressure and stratification.

We will use the 2009 October month over two subdomains representative of different dynamical regimes of the ocean. The first one is centred over the Azores Islands and the North Mid-Atlantic Ridge. The second one is located offshore the North of the US East coast and includes a portion of the Gulf Stream. The Azores domain is characterised by the predominance of topographic features such as the mid Atlantic ridge exhibiting low amplitudes topographic variation over 10 km, and a group of seamount with strong slope and a typical scale of 100 km. Comparatively to the Gulf Stream area, the mesoscale flow is weak. The Gulf Stream domain is marked by a strong mesoscale activity and a large continental slope leading to a flat abyssal plain with a few surrounding seamounts (see Fig. 1 discussed below).

3.2 Filtering and computing methods

In order to obtain the vertical normal modes bases, the mean stratification $\bar{N}^2$ is computed from the time average of temperature and salinity using the nonlinear equation of state from TEOS-10. The Sturm-Liouville problem (6) is then discretised and solved on the staggered vertical grid in each horizontal cell, giving the two modal bases on the T grid, at the centre (in the horizontal) of each cell. From there, the modal amplitude u_n, v_n and p_n are obtained by projecting the corresponding fields $\boldsymbol{u}$ and

p, following (11)-(13). Since the horizontal grid is staggered, the horizontal velocity is located at the edge of each cell. We thus interpolate the base Φ_n before projecting the velocities. Unfortunately, this step induces a loss of orthogonality for the newly interpolated basis. The coefficients determined by innerproduct between the horizontal velocity fields and the interpolated basis are corrected *a posteriori* by inverting the cross-correlation matrix between the interpolated basis and the local basis issued from the Sturm-Liouville problem (6) on the u, v-grid. This allows us to obtain the projection coefficients u_n and v_n defined on the u, v-points. Vertical velocity is then computed using the continuity equation formulated with the discrete scheme employed in the NEMO code [Madec and the NEMO team, 2008].

The next step consists in separating the mesoscale contribution from the semi diurnal internal tide. The latter is extracted by means of a complex demodulation at a central semi-diurnal frequency $\omega = 1.415\times10^{-4}\mathrm{rad\,s^{-1}}$ and a low-pass cutoff cutting period of 3 days. The mesoscale flow is directly low-pass filtered with the same cutting period. The mesoscale slowly-variable buoyancy fields is computed from the daily-averaged temperature and salinity, and the corresponding stratification is then estimated from this buoyancy field and a mean sound speed profile [using standard formula, see *e.g.* Vallis, 2017].

Since our modal decomposition is inaccurate in areas of shallow water, a mask is applied to remove all locations shallower than 300 m in the Azores domain, and 250 m in the Gulf Stream domain. The mask is slightly shallower in the Gulf Stream domain in order to retain the topographic generation occurring at the shelf break.

Since high modes are expected to propagate over shorter distances from their generation site compared to low modes, we usually group the modes 4-10 together, and interpret them as part of dissipative processes in the energy budget. Finally, all terms of equation (15) display small scale patterns, particularly pronounced when the mesoscale and internal tides interact. These patterns are not of particular physical significance for the diagnostics discussed in this paper. Therefore, we apply a Gaussian spatial filter before displaying any term in (15), with a kernel width equal to 25 grid points (a little less than 40 kilometres). This procedure is only applied for map plotting.

4 Results

The energy budget of internal tides in both domains are examined in this section, first by considering the geographical distribution of their generation, propagation and sinks, and secondly by quantifying the spatially integrated and temporally averaged energy budget.

4.1 Life cycle of the internal tide

Both the Azores Islands and Gulf Stream domains are sites of powerful internal tides generation, exposed to contrasted background conditions. The divergence of the energy flux averaged in time over one month (for the period of October 2009) is shown in Figure 1, along with the mesoscale currents at 52 m depth and the topography. In the Azores area, mode 1 energy flux originates from the seamounts and propagates far away (at least 1000 km), indicating a moderate energy loss during the propagation (Fig. 1, top left panel). Modes 2 (not shown) and 3 propagate over shorter distances. All dominant sources and sinks are located around the topography (visible in Figure 1). For the third mode, we find a local loss of energy just next to the generation at the seamount, of the same order of magnitude but smaller value. This property holds for higher modes as well (not shown). In the Gulf Stream domain, in contrast, the input of energy for mode 1 is located at the shelf break, producing a strong offshore beam. This beam manifests strong energy loss as it propagates as can be seen in the negative patch displayed in the mode 1 energy flux divergence, Fig. 1, bottom left panel. A first hot spot of sinks for the mode 1 is directly next to the shelf-break, another being at the encounter with the strong north-eastward current. This beam is also refracted by the Gulf Stream, a behaviour previously reported in Duda et al. [2018]. As we will show in the next section (*cf.* Figures 3 and 2), this loss of energy is mainly caused by the advection terms in equation (15) and is largely converted in mode 2 energy. Mode 3 (Fig. 1, bottom right panel) displays a more complex repartition of sources and sinks, with an overall gain of energy at and near the shelfbreak and an overall loss of energy further away from the land, where it encounters the current. The sources and sinks of energy from modes 1 and 3 are therefore much less localised around the prominent topographic feature than in the Azores domain, and clearly exhibit strong interactions with the mesoscale currents.

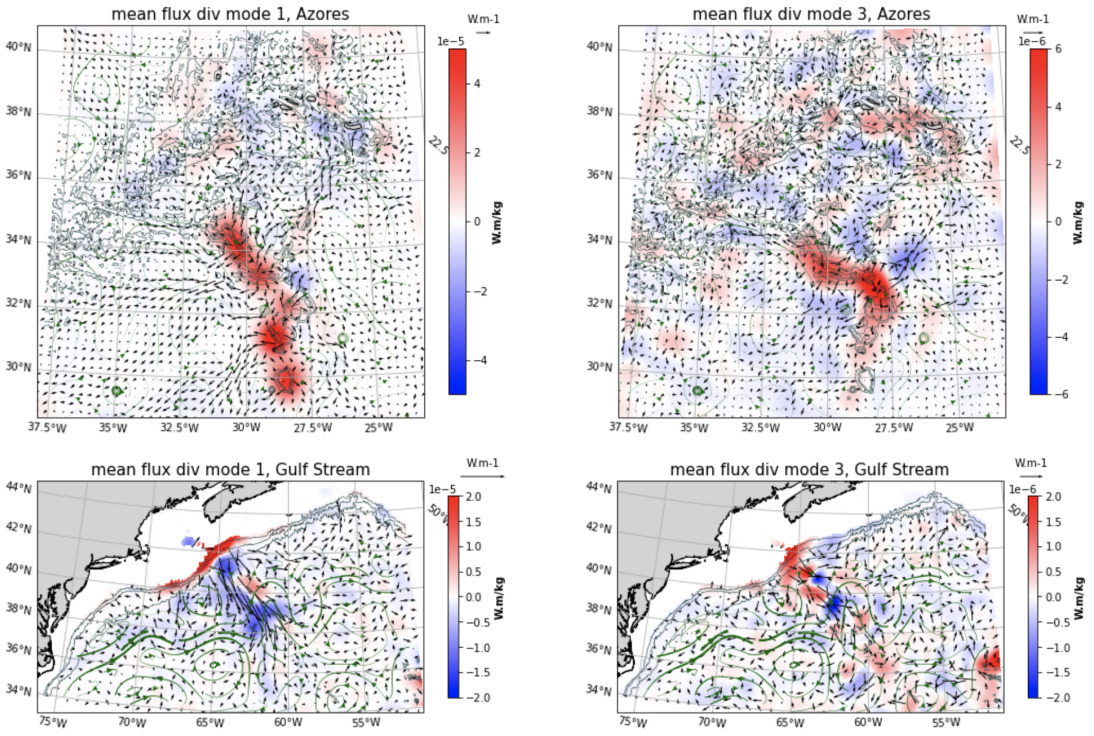

Figure 1: One-month average of the horizontal energy flux divergence for mode 1 (left column) and mode 3 (right column), for the Azores domain (top) and the Gulf Stream domain (bottom). A positive value indicates a gain of energy for the mode. Black arrows show the square root of the corresponding modal horizontal energy flux. A spatial Gaussian filter with a half modal wavelength kernel has been applied on these fields in order to remove the local alternate of positive and negative values and make the plot cleaner. Green streamlines indicate, qualitatively, the mesoscale horizontal currents at 52 m depth, and isobaths at 1000 m, 2000 m and 3000 m are superimposed in grey contours.

4.2 Importance of the different contributions in the energy transfers

We now focus on quantifying the causes of the multiples interactions of the internal tide with its surrounding which results in the pattern in the energy flux divergence previously described (Fig. 1).

4.2.1 4.2.1 Detailed view of coupling terms.

To this aim, the modal energy budget (15) is integrated over the two domains considered, averaged over the October month and the different contributions are displayed under their matrix form in figure 3. The matrix are decomposed into their anti-symmetric part (upper triangle) denoting a transfer of energy from mode to mode, referred afterwards as scattering, and symmetric part (diagonal plus lower triangle) showing sources or sinks for the internal tide. We have only plotted terms of (15) that are of first order for at least one mode in one domain.

Amongst these terms, the topographic contribution is at least one order of magnitude higher than all others for the barotropic mode in both domains and for the first baroclinic mode in the Azores domain. However, for the Gulf Stream area, the advection coupling becomes of similar magnitude for the first mode and exceed the topographic scattering for modes 2 and 3. In the Azores domain, this is non negligible for modes 2 and 3 but never exceeds the topographic contribution. In this region, the second largest contribution is given by the variable stratification coupling for the baroclinic modes. In The Gulf Stream area, the mesoscale vertical shear production and the horizontal buoyancy gradient loss are also of first order. However, as already found in Kelly and Lermusiaux [2016], these two terms seem to compensate each other leaving a near zero energy gain for mode 1 – which the authors explained as resulting from the thermal wind balance holding for the background flow. The same phenomenon approximately occurs for higher modes, *cf.* Figure 2: the lower triangles of buoyancy and shear matrix cancel out.

These dominant processes are dominated by their anti-symmetric part. The topographic contribution is purely anti-symmetric by construction, while the sum of the symmetric part for a given mode for the advection coupling is always smaller than 10% of the sum of the anti-symmetric part when this term is significant in regard to the topographic scattering. This quantity never exceeds 20% for the variable stratification coupling in the Azores domain. For the Gulf Stream domain however, it is close to one for the first baroclinic mode, indicating that symmetric and antisymmetric parts have comparable magnitudes. The background flow shear and buoyancy gradient couplings have a dominant symmetric part, but these two terms are cancelling each others. Last, if we sum all the contributions of the modal energy budget (15), the symmetric transfer of energy is found to be worth less or equal to 14% for modes 1 , 3 in both domains and 2 in the Azores one. Therefore, the interaction between the mesoscale circulation and the internal tides mainly contribute to a scattering of modes equivalent to the one produced by the topography without exchanges between the internal tides and the mesoscale circulation and buoyancy field.

As a last comment, Figure 2 shows that topographic scattering is the only process that significantly transfers energy between non-neighbouring modes. For the other dominant processes, the energy transfer toward non-neighbouring modes is one order of magnitude lower than the one toward a neighbouring mode, except for the variable stratification coupling in the Gulf Stream area. For the mesoscale contributions, this implies that only the third mode is able to transfer energy toward what we consider as part of dissipative processes.

4.2.2 4.2.2 Modal energy budget

We are now looking at a more aggregated view of (15) thanks to figure 3 which shows the modal energy budget of mode 1, 2 and 3 for both domains. Here we have separated the energy transfers with the following decomposition:

Topographic Scattering : $C_{nm} = p_m \boldsymbol{u}_n \cdot T_{nm} - p_n \boldsymbol{u}_m \cdot T_{mn}$

Advection of the interal tide : $A_{nm} = \boldsymbol{u}_m \cdot (U_{mn} \cdot \boldsymbol{\nabla} \boldsymbol{u}_n) - \boldsymbol{u}_m \cdot \boldsymbol{u}_n U^{\Phi}_{mn} + \frac{p_m}{c_m^2} U^p_{mn} \cdot \boldsymbol{\nabla} p_n$

Shear of background flow : $\nabla U_{nm} = \boldsymbol{u}_n \cdot U^{\boldsymbol{\nabla}}_{mn} \cdot \boldsymbol{u}_m + \boldsymbol{u}_m \cdot U^z_{mn} w_n$

Horizontal gradient of buoyancy field : $\nabla B_{nm} = \frac{p_m}{H c_m^2} \boldsymbol{u}_n \cdot (\bar{B}_{mn} + B_{mn})$

Surface contribution and advection of the mean stratification profile : $S_{nm} = -\frac{p_m}{H c_m^2} g \varphi_m(\overline{\eta}) \boldsymbol{U_h}(\overline{\eta}) \cdot \boldsymbol{\nabla} \tilde{\eta} - \frac{p_m}{c_m^2} \sum_n p_n \left\langle \varphi_m, \boldsymbol{U}_h \cdot \boldsymbol{\nabla}_h \left(\frac{\bar{N}^2}{c_n^2} \varphi_n \right) \right\rangle$

Variable stratification : $N_{nm} = \frac{p_m}{c_m^2} w_n \left\langle \varphi_m, N^2 \varphi_n \right\rangle$

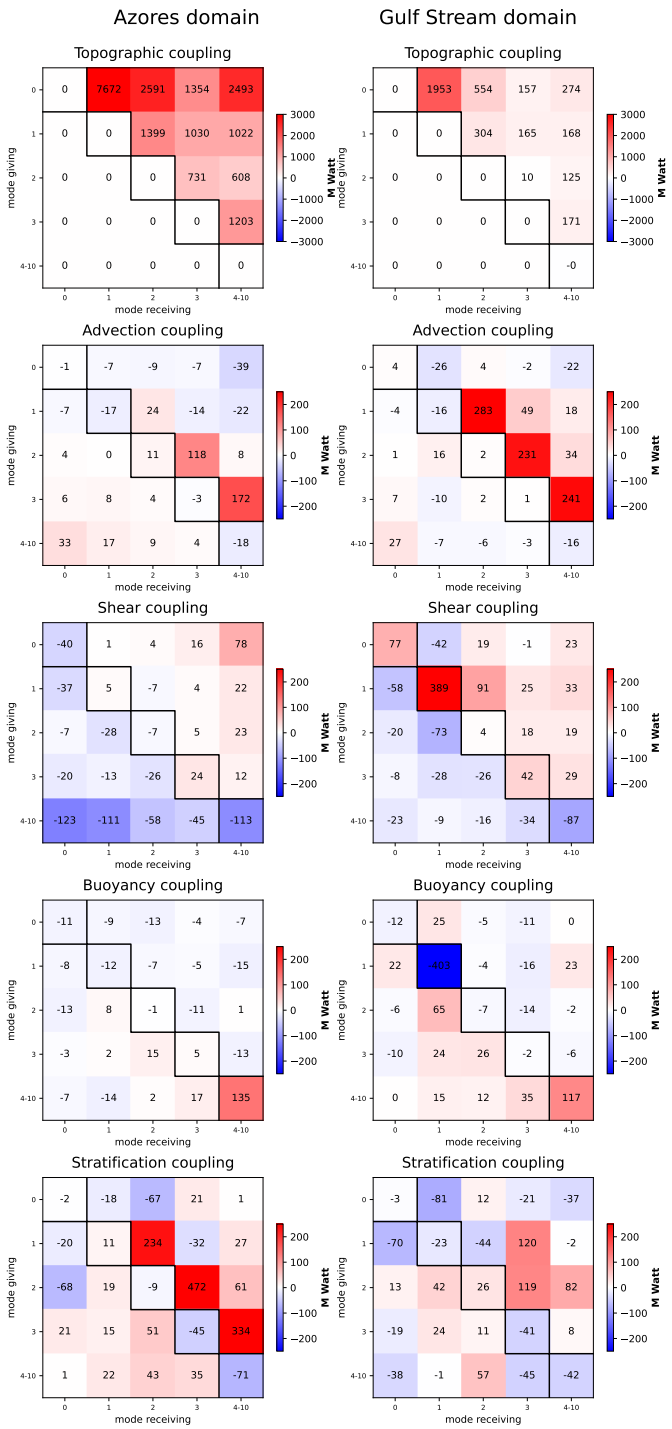

Figure 2: Matrices K_{nm} summarising the mean energy transfer integrated over the whole subdomains between a mode n (row) and a mode m (column). The upper-right triangle is the anti-symmetric part, and the lower-left triangle (diagonal included) the symmetric part. The sign convention follows eq. (15): a positive value indicates a gain of energy for the reference – "receiving" – mode m from n mode and conversely. Modes 4 to 10 are grouped together. From top to bottom are the coupling caused by the topography, the internal tide advection by the background flow, the terms implying the horizontal and vertical shear of the background flow and the term implying the gradient of the buoyancy field (both variable and annual mean). Notice the different range of values in the colorbar for the topographic coupling terms compared to the other ones.

We also have separated the symmetric part (*) of the antisymmetric one, and have furthermore divided the latter into an energy exchange coming from lower modes, and an energy exchange going from higher modes (**). The flux coming from lower modes is again divided into an energy transfer coming from the barotropic mode (****), and transfers coming from the baroclinic ones (***). A positive value means a transfer of energy toward the mode of interest.

If we consider i the index of the mode of interest and A_{nm} the energy transfer matrix already separated into symmetric and antisymmetric part as in figure 2, then we have :

$**** = A_{0i}$
$*** = \sum_{n=1}^{i-1} A_{ni}$
$** = -\sum_{n=i+1}^{4} A_{in}$
$* = \sum_{n=0}^{i} A_{in} - \sum_{n=i+1}^{4} A_{ni}$

Comparing the integrated value of the energy divergence flux, the Gulf-Stream domain is overall less energetic than the Azores domain: mode 1 has a divergence around 4 time larger in the last domain than in the first and modes 2 and 3 are also more energetic in the Azores area. In the results displayed in figure 3, the mode 1 in the Gulf-Stream domain is the only one to have an overall negative energy flux divergence.

The barotropic mode has an importance in the energy budget of mode 1 to 3 only through the topographic scattering, and is dominant in the energy budget of mode 1 for both areas. However, it becomes less important for modes 2 and 3, with a contribution to the topographic scattering toward mode 3 inferior to the one caused by modes 1 and 2, but still significant.

Among the first order energy transfers exposed in all panels of figure 3, none transfers energy from small scale to large scale. Mesoscale and topographic couplings therefore create a forward energy cascade.

Last, figure 3 enables identifying the terms of the modal energy budget (15) that are of negligible importance. The advection of ssh and stationary stratification are negligible, which justifies gathering these terms in equation (15) in a small residual term. Similarly, the astronomical tidal potential (not included in Figure 3) only projects weakly on the baroclinic modes. The mean of temporal variations of potential and kinetic energy are also small: one month is enough to flatten the two weeks periodic variation introduced by the spring neap cycle.

5 Conclusion

The semidiurnal internal tide energy budget was characterised based on a vertical mode decomposition, allowing a detailed investigation of the energy transfers amongst different vertical scales – and associated horizontal scales – of the internal tide field. We showed that the Azores area, a region of weak mesoscale activity and strong topographic features, is essentially dominated by the topographic induced energy transfer from low to higher modes. While this effect is dominant for low modes, variable stratification and – to a lesser extent – advection of the internal tide by the mesoscale flow become of similar importance for high modes (equal or larger than 2). Some questions remain concerning the precise role of the variable stratification, in relation with the definition of the modal basis expansion and how this definition would change the energy exchanges between modes. In the Gulf Stream area, advection of the internal tide by the background flow is as significant as the topographic scattering – the transfer of energy caused by the advection becoming more important than the one caused by topographic scattering starting from mode 2 –, while the variable stratification term is less important. However, the net impact of the mesoscale circulation on the energetic of internal tide is mainly limited to a scattering of energy from the low to high-order modes. In comparison, exchange of energy between the internal tide and the mesoscale fields are negligible: the energy exchanged by modes 1 to 3 with the background is always less than 14% of the total energy transfer for the respective mode.

The type of modal analysis conducted in the present paper on a high resolution primitive equation simulation is able to give some insights on the energetic impact of mesoscale circulation and its associated buoyancy field on the internal tide and the transfer of energy from the astronomical tide toward dissipation. This work could be extended by investigating the deep water mixing caused by these interactions. We have in particular overlooked for now the internal tide dissipation, but it is worth investigating in the near future.

Finally, the temporal variability of mesoscale - internal tides interactions will also be studied in the near future.

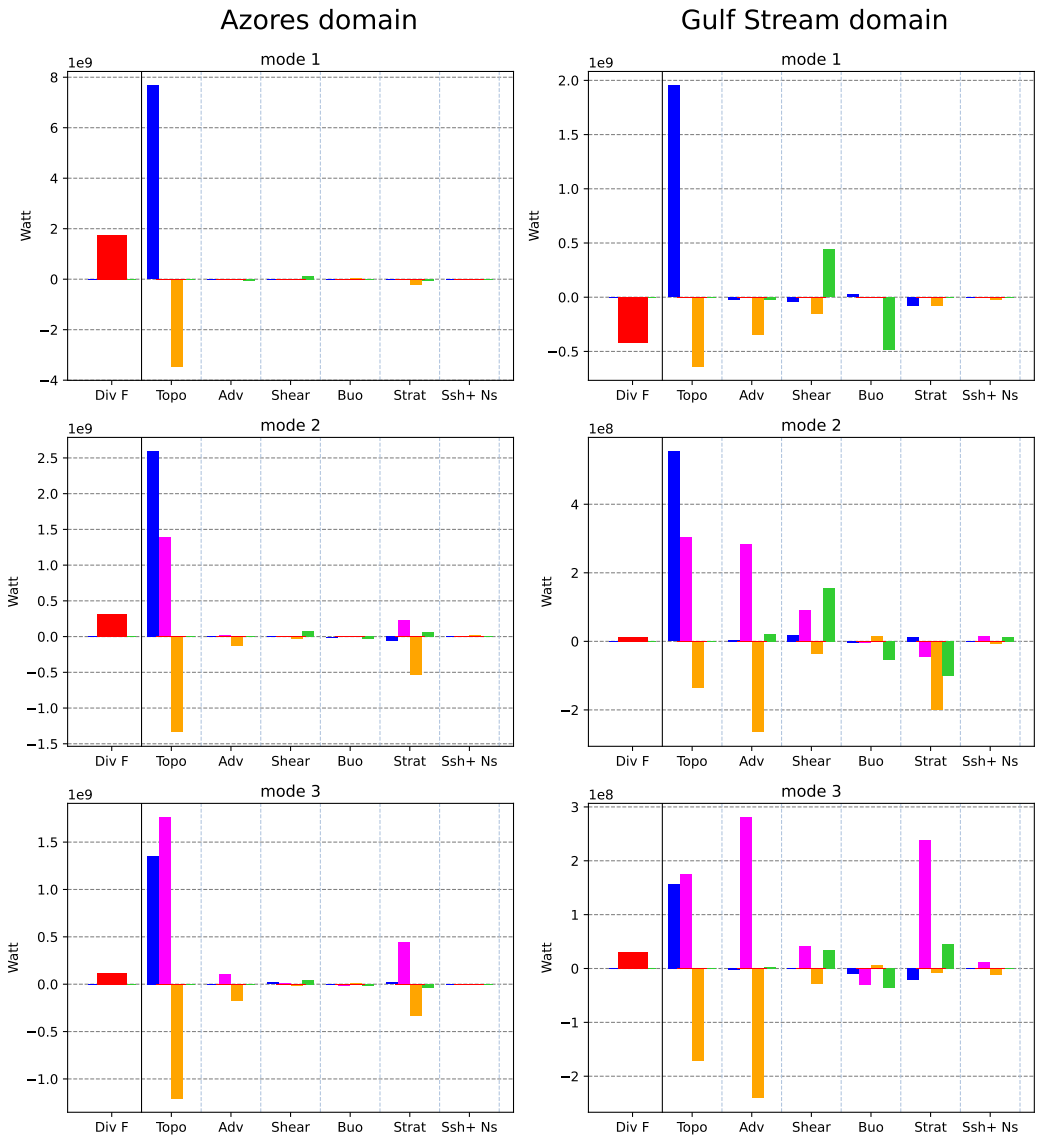

Figure 3: Mean modal budget for modes 1 (top), 2 (middle row) and 3 (bottom) for the Azores domain (left) and the Gulf Stream (right) domains, as described by equation (15). The divergence of the modal flux is plotted in red, while others contributions are separated into the symmetric part (green) and the anti-symmetric part where interaction with lower modes and with higher modes (orange) are separated. The anti-symmetric part coming from low modes is furthermore separated into fluxes coming from the barotropic mode (blue) and fluxes coming from the baroclinic modes (fuchsia). A positive value means a gain of energy for the mode. Processes taken into account are Topo : C_{nm} , Adv : A_{nm}, shear : ∇U_{nm}, ssh + Ns : S_{nm}, Buo : ∇B_{nm} , Strat : N_{nm}.

References

B. K. Arbic, A. Wallcraft, and E. Metzger. Concurrent simulation of the eddying general circulation and tides in a global ocean model. *Ocean Modelling*, 32:175–187, 2010.

M. Ballarotta, C. Ubelmann, M-I. Pujol, G. Taburet, F. Fournier, J-F. Legeais, Y. Faugère, A. Delepoulle, D. Chelton, G. Dibarboure, and N. Picot. On the resolutions of ocean altimetry maps. *Ocean science*, page 1091–1109, 2019.

L. Brodeau, J. Le Sommer, and A. Albert. Ocean-next/eNATL60: Material describing the set-up and the assessment of NEMO-eNATL60 simulations. Zenodo, September 2020.

T. F. Duda, Y.-T. Lin, M. Buijsman, and A. E. Newhall. Internal tidal modal ray refraction and energy ducting in baroclinic gulf stream currents. *Journal of Physical Oceanography*, 48, 2018.

M. Dunphy and K. G. Lamb. Focusing and vertical mode scattering of the first mode internal tide by mesoscale eddy interaction. *Journal of Geophysical Research: Oceans*, 33:523–536, 2014.

A. E. Gill. *Atmosphere-Ocean dynamics*. International Geophysics Series, Academic Press, Vol 30, 1982.

S. M. Kelly. The vertical mode decomposition of surface and internal tides in the presence of a free surface and arbitrary topography. *American Meteorological Society*, Volume 46, Issue 12:3777–3788, 2016.

S. M. Kelly and P. F. J. Lermusiaux. Internal-tide interactions with the gulf stream and middle atlantic bight shelfbreak front,. *Journal of Geophysical Research: Oceans*, 121:6271–6294, 2016.

G. Madec and NEMO ocean engine the NEMO team. *Note du Pôle de modélisation*. Institut Pierre-Simon Laplace (IPSL), France,, No 27, ISSN No 1288-1619., 2008.

W. Munk and C. Wunsch. Abyssal recipes ii: energetics of tidal and wind mixing. *Deep-Sea Research*, Volume 45, Issue 12:1977–2010, 1998.

Y. Pan, P. J. Haley, and P. J. F. Lermusiaux. Interactions of internal tides with a heterogeneous and rotational ocean. *Journal of Fluid Mechanics*, 920, 2021.

A. L. Ponte and P Klein. Incoherent signature of internal tides on sea level in idealized numerical simulations. *Geophysical Research Letters*, Volume 42:1520–1526, 2015.

G. K. Vallis. *Atmospheric and Oceanic Fluid Dynamics: Fundamentals and Large-Scale Circulation*. Cambridge University Press, 2017.

E. D. Zaron, R. C. Musgrave, and G. D. Egbert. Baroclinic tidal energetics inferred from satellite altimetry. *Journal of Physical Oceanography*, page 1015–1032, 2022.

Z. Zhao, M. H. Alford, J. B. Girton, L. Rainville, and H. L. Simmons. Global observations of open-ocean mode-1 M2 internal tides. *Journal of Physical Oceanography*, 46:1657–1684, 2016.